Anisotropic elastic properties of synthetic and natural fibers determined by micro-Brillouin light spectroscopy

Fehima Ugarak [1], Fanny Pelisson [1], Marina Raschetti [1], Vincent Placet [1], Pauline Butaud [1], Morvan Ouisse [1], Alexis Mosset [1], and Vincent Laude [1]

[1] Université Marie et Louis Pasteur, SUPMICROTECH, CNRS, institut FEMTO-ST; 25000 Besançon, France

E-mail: vincent.laude@femto-st.fr

Abstract. Synthetic and natural fibers with diameters in the range of a few tens of micrometers can be routinely fabricated. Because of the intricate microstructure of the fibers, however, their elastic properties remain poorly understood. In this study, we employ micro-Brillouin light spectroscopy (micro-BLS) to explore direction-dependent acoustic phonon propagation in amorphous E-glass, synthetic silk, polyamide 11 (PA11), and flax fibers. The technique is non-invasive and non-destructive, and is an alternative to static mechanical tests. The observable frequency shifts of laser light resulting from Brillouin scattering from hypersonic acoustic phonons of the fiber are in a few 10-GHz range. We determine the full elastic tensors and the optical anisotropy, assuming only transversely isotropic symmetry at the optical wavelength scale. The obtained elastic constants are compared with values reported in the literature for similar materials.

Keywords: micro-Brillouin light scattering, elastic tensor, fibers, transverse isotropy

Submitted to: *J. Phys. D: Appl. Phys.*

1. Introduction

Natural fibers, including plant fibers, enter the fabrication of sustainable composites. Recent research has illuminated their intricate elastic properties. By mapping longitudinal moduli, scientists have revealed spatial heterogeneity and anisotropic behavior. These findings have broad implications across various fields such as materials engineering and design [1], textile industry, biomechanics and medical devices, forensic science, non destructive testing (NDT) and environmental monitoring. The elastic properties of fibers are typically investigated through destructive and invasive analysis methods. Recent studies using Brillouin Light Scattering (BLS) micro-spectroscopy, however, have yielded promising results. This non-invasive, all-optical technique maps the complex longitudinal modulus of fibers, revealing significant spatial heterogeneity and anisotropic mechanical properties. Notably, investigations on viscose fibers and bleached softwood pulp [1] demonstrated a regular pattern of modulus variation normal to the fiber axis. A similar study [2] focused on a micro-structured composite system comprising wool fibers (approximately 15 µm in diameter) embedded in a 30 µm thick epoxy film affixed to a reflective silicon substrate. The elastic constants of cellulosic viscose fibers were determined [3] combining two different scattering processes and directions with only one scattering geometry. Wang et al. [4] estimated the full elastic tensor and the ordinary and extraordinary refraction indices of spider silk by a combination of measurements in different scattering geometries. Recently, Aluculesei et al. characterized Bombyx mori silkworm silk fiber following a similar methodology [5].

There is hence a strong interest in obtaining the elastic properties of other synthetic and natural fibers. We specifically consider in this work E-glass, polyamide 11, flax, and synthetic silk. E-glass fibers were originally developed for electrical insulation and are widely produced industrially for applications in textile and composite materials. They are produced as multifilament bundles, with filament diameters ranging from 3 to 20 µm. Polyamide 11 (PA11), also known as Nylon 11, is a versatile synthetic polymer derived from renewable resources, primarily castor oil. Polymerized amides, linked by peptide bonds, are thermoplastic materials known for their high tensile strength, good creep resistance, and outstanding resistance to abrasion, chemicals, and heat [20]. PA11 fibers are used in automotive processing, aerospace, healthcare, electronics, sports equipment, and coatings due to their lightweight, durability, chemical resistance, and bio-compatibility. Silk exhibits exceptional mechanical properties, including high tensile strength and significant extensibility, positioning it among the toughest materials known [21, 22, 23]. The excellent properties of flax fibers made them very well recognized in a wide range of applications. The primary use of this fiber is in the production of textiles, such as clothing or linens, due to its strength, durability, and comfort. Flax fibers are also employed in the creation of ropes and high-quality paper products, but also as a reinforcement in composite materials for building and automotive applications. Flax cultivation is environmentally friendly, requiring low inputs of water, pesticides, and fertilizers, making it a sustainable choice compared to synthetic fibers [24, 25]. Further details about harvesting, structure and composition of flax fibers are given by Richely et al. [26] and Bourmaud et al. [27].

Despite their intricate microstructures, the complete elastic properties of these fibers remain poorly understood. Traditional stress-strain experiments only measure the axial Young's modulus. In this study, micro-BLS is employed to explore direction-dependent phonon propagation in E-glass, silk, PA11, and flax fibers, determining their full elastic properties and their optical birefringence, employing only measurements in the backscattering configuration in two different incidence planes, either containing or orthogonal to the fiber axis, plus an additional measurement along the fiber axis. The value of the ordinary optical index is hence assumed to be known independently and its value is retrieved from the literature. Our findings represent one of the first demonstrations of determination of anisotropic Young's moduli, shear moduli, and Poisson's ratio for synthetic and natural fibers using micro-BLS.

In the following, we first describe in Section 2 the fibers we considered and methods we used. Micro-Brillouin light scattering gives experimental access to the frequencies of acoustic phonons that are matched with the incident optical wavevector. From a set of measurement data obtained in two different incidence planes and along the fiber axis, we discuss how the full elastic tensor can be retrieved from Brillouin frequencies. Other elastic constants can then be deduced from the elastic tensor. In Section 3 we discuss

Fiber	Mass density ρ (kg m^{-3})	Poisson's ratio ν	Ordinary optical index n_o
E-glass	2570 (2550 – 2600) [6, 7]	0.2 – 0.3 [6]	1.56 [6]
PA11	1045 [8]	(0.34 – 0.5) [9, 10, 11]	1.52 [8]
Silk	1400 [12]	(0.1 – 0.5) [13, 11, 5]	1.5587 [14]
Flax	1500 [15]	(0.2 – 0.5) [16, 17, 18]	1.58 [19]

Table 1. Some material constants for the fiber samples considered in this work, as found in the literature.

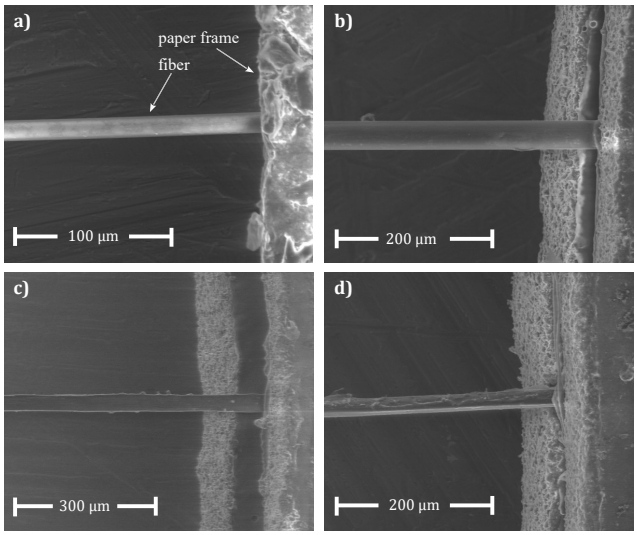

Figure 1. Scanning electron microscope images of single fibers fixed onto a paper frame: a) E-glass with diameter 13.4 µm, b) PA11 or polyamide with diameter 36.8 µm, c) synthetic silk with diameter 23.8 µm, and d) flax with diameter 17.0 µm.

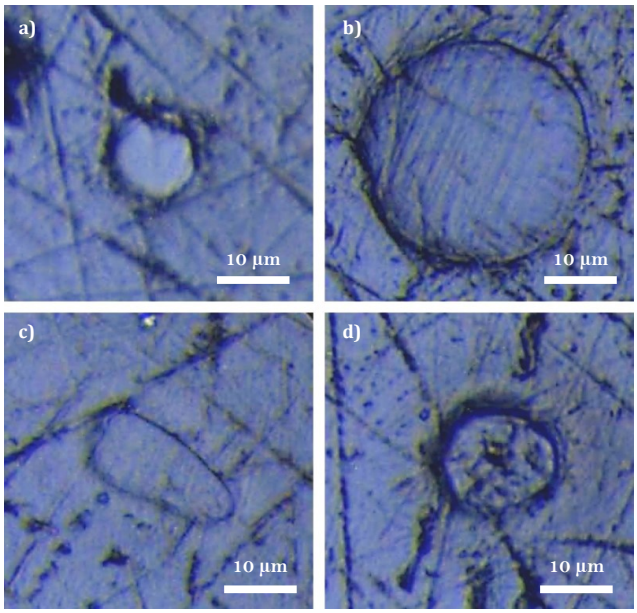

Figure 2. Optical microscope images of single fibers embedded in epoxy resin: a) E-glass, b) PA11, c) synthetic silk, and d) flax.

in sequence the results obtained for four types of fiber: E-glass, PA11, silk, and flax. We finally conclude in Section 4 on the values of the elastic constants obtained and why they may differ from results in the literature obtained from tensile or low-frequency vibration measurements.

2. Materials and Methods

2.1. Fiber samples

We considered four types of fiber samples, covering a wide range of fiber categories, as listed in Table 1. E-glass fiber typifies inorganic fibers [6]; polyamide (PA11) is a synthetic organic fibers [8]; silk exemplifies animal-derived fibers [12]; flax serves as a representative of plant fibers [15]. The synthetic silk fiber considered is a regenerated cellulose fiber (Marzotto), thus classified as a polymeric fiber; a single fiber is manually extracted from a bundle and tested as such, without further processing. Flax fibers were individually isolated from an unidirectional mat (flaxtape, Ecotechnilin), whereas other fibers were extracted from unidirectional fabrics. All fibers were then carefully arranged within a paper frame, see Figure 1. All samples were stored and measured under ambient conditions (temperature 294 K, atmospheric pressure and humidity range 60 – 80%).

For axial BLS measurements, we further prepared samples of the four fibers embedded in an epoxy matrix, cut normally to the fiber axis, see Figure 2. The fibers are placed in a paper frame immediately after extraction from a bundle, while awaiting embedding. Once all the fibers are positioned, a Greenpoxy (SICOMIN) matrix is prepared and the fibers are embedded within it. The system is then left to cure for 48 hours at room temperature and atmospheric pressure. The sample finally undergoes a precise polishing protocol, ensuring that the fiber is flat and parallel to the matrix surface. We assume that this technological operation has a negligible effect on the mechanical properties of the fibers, compared to their free versions, but this potential effect could not be precisely quantified.

E-glass fiber is amorphous and hence elastically and optically isotropic; there are thus only two independent elastic constants in this case. For all other

fibers, the expected behaviour is transversely isotropic symmetry with respect to the fiber axis, a sub-case of orthotropy. This symmetry implies five independent elastic constants, which we take to be c_{11}, c_{12}, c_{13}, c_{33} and c_{44} [28, 29, 30], and two independent optical indices. Prior knowledge of at least one refractive index is essential for BLS measurements in the backscattering geometry. In the literature, the refractive index for E-glass fiber is known and at $\lambda = 532$ nm, $n_o = n_e = 1.56$ [6]. For the other fibers, which are all optically anisotropic, we take the ordinary index from the literature (see Table 1) and fit the extraordinary index from micro-BLS measurements. The birefringence $\Delta n = n_e - n_o$ is indeed rather small but varies depending on the conditions of preparation of the fibers. When converting from Brillouin frequency shifts to elastic constants, the mass density is required and is not provided by BLS. The values listed in Table 1 for mass densities are thus used. Hence, in the absence of more precise information regarding uncertainties pertaining to index of refraction and mass density, we consider the values given in Table 1 as ideal. As a consequence, uncertainties on elastic constants given in later sections are underestimated in comparison to actual uncertainties. This limitation does not apply to the Brillouin frequencies that are the main observables in this work.

2.2. Micro-Brillouin light scattering

Brillouin spectroscopy has emerged as a cutting-edge analytical technique in the field of biophotonics research and applications. Operating at a microscopic scale and within the GHz spectral range, it offers a novel spatial and frequency perspective for assessing material elasticity [2]. Thermally excited acoustic phonons at room temperature carry information on the mechanical properties of the materials within whom they propagate. Variations of the dielectric constant induced by spontaneous acoustic phonons create a periodic grating of refractive index fluctuations on which laser light can diffract. In the case of a monochromatic incident light beam, the grating periodicity is determined by the acoustic wavelength and results in a frequency shift f of the backscattered light in the GHz range. The elastic constants at hypersonic frequencies are probed from the Brillouin peak frequency shifts.

To evaluate the mechanical properties of the fibers, we used a single longitudinal mode (green) laser with the wavelength $\lambda_0 = 532$ nm in air (Figure 3). The incident light beam passes through a polarizing beam splitter (PBS) and reflects on mirrors M1 and M2, is expanded through the beam expander and reflects on mirror M3. A $\lambda/4$ wave plate provides circular polarised light. Through the 20× objective lens with numerical aperture 0.42 the incident probe light is focused on the sample, with an input power of less than 4 mW, and creates a focal spot size of 2 µm. Long integration times at low laser power are selected so that thermal equilibrium can be reached; we checked the stability over time of the Brillouin response but the sample temperature was not specifically monitored. Backscattered light is collected by the same objective and detected by a six-pass tandem Fabry−Perot interferometer (TFP2-HC, JRS Instruments). Bulk phonons with wavevector $q = k_s - k_i$ are probed, where k_i and k_s are the wavevectors of incident and scattered light, respectively. Because of the small diameter of the fibers, that varies between 10 and 40 µm (Figure 1), a CCD camera was used in combination with a LED light source for positioning the laser spot onto the fiber.

As Figure 3 depicts, measurements were conducted in the backscattering geometry either on a single fiber embedded in epoxy (inset 1) or on a single fiber fixed in a paper frame (insets 2 and 3). Data analysis was performed using a homemade Matlab code. The reference frame is attached to the laboratory and is noted (x_1, x_2, x_3). The fiber sample can be rotated in space around two axes; as a result the material frame (X, Y, Z) is different from the reference frame. The fiber axis is always taken as material axis Z, and axes X and Y are equivalent per axial symmetry of the fiber. As a result of these definitions, in Figure 3 the reference frame aligns with (X, Y, Z) for inset 1, $(Z, -Y, X)$ for inset 2, and (Y, Z, X) for inset 3.

In the backscattering geometry, the Brillouin frequency shift f is related to the phase velocity of acoustic phonons v and to the refractive index n through the phase-matching condition

$$f = \frac{2nv}{\lambda_0}. \tag{1}$$

Both the refractive index and the phase velocity depend on the angle of incidence and on the orientation of the sample. The interferometer selects a linear light polarization noted H that is aligned with the x_2 axis of the reference frame. The polarization of incident light decomposes along axes H and V, with V aligned with the x_1 axis and thus in the incidence plane. For axial incidence (inset 1), both H and V correspond to ordinary light polarization. For incidence in the (XZ) plane (inset 2), H (V, respectively) is ordinary (extraordinary, resp.) light polarization. For incidence in the (XY) plane (inset 3), H (V, resp.) is extraordinary (ordinary, resp.) light polarization.

2.3. Fit of the elastic tensor and birefringence

The full elastic properties are identified by an inverse method from experimental data. Parameter

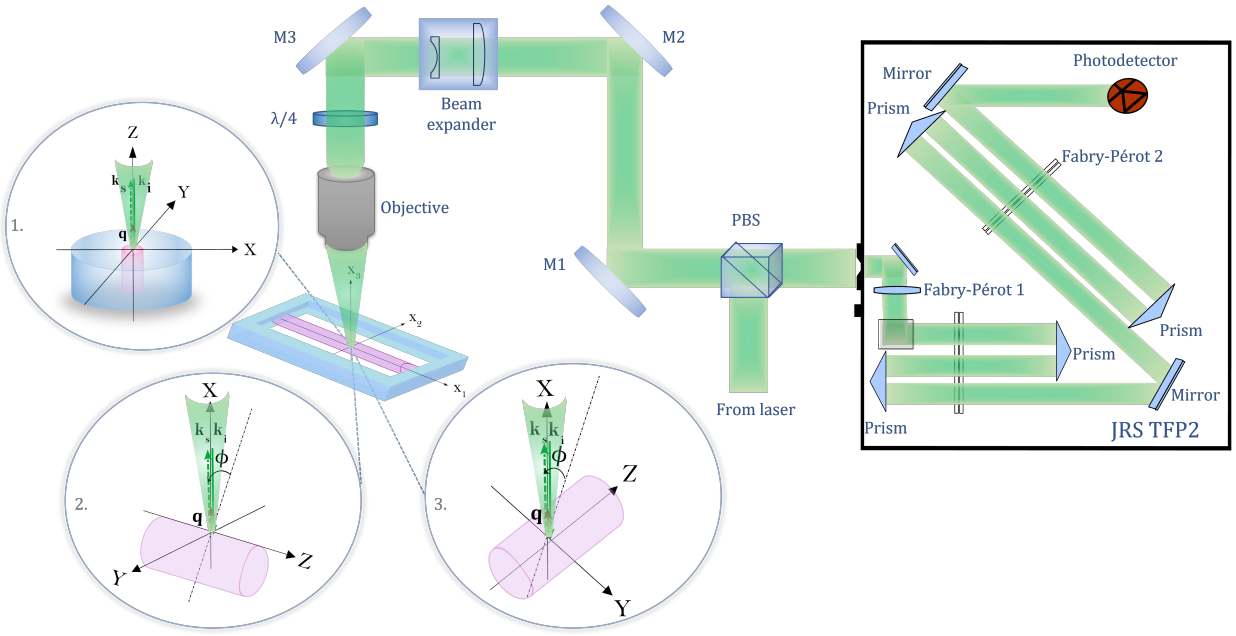

Figure 3. Micro-Brillouin light scattering experiment and sample positioning. The insets depict the scattering geometry for the three incidence conditions considered. PBS: polarizing beam splitter; M1, M2, M3: mirrors.

estimation is performed employing a homemade code written in the Julia programming language and using the Levenberg-Marquardt algorithm to minimize the distance between experimental and computed Brillouin frequency shifts [31]. It is well-known that elastic stiffness constants are coupled with sound velocities through the Christoffel's equation [32]. Assuming transversely isotropic symmetry, the shape of the elastic tensor is (see Appendix A) [33]

$$c_{\alpha\beta} = \begin{bmatrix} c_{11} & c_{12} & c_{13} & 0 & 0 & 0 \\ c_{12} & c_{11} & c_{13} & 0 & 0 & 0 \\ c_{13} & c_{13} & c_{33} & 0 & 0 & 0 \\ 0 & 0 & 0 & c_{44} & 0 & 0 \\ 0 & 0 & 0 & 0 & c_{44} & 0 \\ 0 & 0 & 0 & 0 & 0 & c_{66} \end{bmatrix} \tag{2}$$

with $c_{66} = (c_{11} - c_{12})/2$. Knowledge of the optical relative dielectric tensor is also necessary for fitting Brillouin frequencies and expresses as

$$\epsilon_{ij} = \begin{bmatrix} n_o^2 & 0 & 0 \\ 0 & n_o^2 & 0 \\ 0 & 0 & n_e^2 \end{bmatrix} \tag{3}$$

with n_o the ordinary index of refraction and n_e the extraordinary index of refraction. For PA11, silk and flax fibers, 5 independent elastic constants and the value $\epsilon_{33} = n_e^2$ of the optical dielectric tensor are considered as variables, for a total of 6 independent variables. Considering that the value $\epsilon_{11} = \epsilon_{22} = n_o^2$ is known beforehand, the birefringence $n_e - n_o$ is obtained in the process. As we will illustrate in Section 3, measurement of Brillouin frequency shifts for phonons propagating in incidence planes (XZ) and (XY) allows us to estimate the full elastic tensor. The $m = 6$ independent variables are arranged in a vector $\mathbf{p}$. The number of experimental Brillouin peak frequencies f_j is M $(j = 1, \cdots, M)$. The fitting error that is minimized is

$$e(\mathbf{p}) = \sum_{j=1}^{M} (f_j - f(\alpha_j, \psi_j, \phi_j; \mathbf{p}))^2 / f_j, \tag{4}$$

where (ψ_j, ϕ_j) are the sampling angles, $\alpha_j \in \{\text{QL}, \text{QS}, \text{S}\}$ is the classification of the acoustic phonons (quasi-longitudinal, quasi-shear, or pure shear), and $f(\alpha, \psi, \phi; \mathbf{p})$ is a function giving the theoretical Brillouin frequencies (see Appendix B for explicit formulas giving the phase velocity of each phonon as a function of the angle of incidence). As per Eq. (1), the Brillouin frequency shift is proportional to the index of refraction and the phonon velocity; through Christoffel's equation $v = \sqrt{c/\rho}$, with c an effective elastic tensor value. As a whole, the fitted material parameters depend on the assumed value for n_o and ρ. The fitting error has units of frequencies (GHz). The Levenberg–Marquardt algorithm is used to obtain the minimum of the error e, starting from a given initial set of material constants. The standard deviation of each fitted parameter is evaluated as

$$\sigma_i = \sqrt{\frac{e(\mathbf{p}_0)}{DV_p^{-1}[i,i]}}, \; i = 1, \cdots, m \tag{5}$$

where $e(\mathbf{p}_0)$ is the remaining error at the minimum $\mathbf{p}_0$, V_p is the Hessian matrix at the minimum, and $D = M - m + 1$ stands for the number of degrees of freedom. As a note, the standard deviations are indicators for the quality of the fit, expressed in the same physical units as the fitted material parameters.

The fitting model just described assumes that each observed Brillouin peak can be attributed to a given bulk phonon. Appendix C specifically discusses the photoelastic couplings active for each phonon.

2.4. Conversion between elastic tensor and elastic constants

In the case of the E-glass fiber, due to isotropy, the elastic constant c_{11} is the only one that can be measured in the backscattering configuration. c_{11} is linked to the longitudinal phase velocity by the relation

$$v_L = \sqrt{\frac{c_{11}}{\rho}}, \tag{6}$$

with ρ the mass density. For such an isotropic material the relation between c_{11} and Young's modulus E is given by

$$E = \frac{c_{11}(1+\nu)(1-2\nu)}{(1-\nu)} \tag{7}$$

with Poisson's ratio ν. For a complete characterization of elastic constants, two independent elastic constants are required (e.g., c_{11} and c_{44}). Since shear phonons are not observed, however, c_{44} is not accessible and the value of Poisson's ratio must be assumed for the determination of E, or the converse.

For PA11, silk and flax fibers, the five independent elastic constants c_{11}, c_{12}, c_{12}, c_{33}, and c_{44} are estimated by the fit procedure described in the previous section. Mechanical moduli and Poisson's ratio can then be derived from the elastic tensor as follows [3]. The longitudinal Young's modulus is

$$E_L = E_z = c_{33} - \frac{2c_{13}^2}{c_{11}+c_{12}}. \tag{8}$$

The transverse Young's modulus is

$$E_T = E_x = E_y = \frac{(c_{11}-c_{12})(c_{11}c_{33}+c_{12}c_{33}-2c_{13}^2)}{c_{11}c_{33}-c_{13}^2}. \tag{9}$$

The in-plane shear modulus is

$$G_{xy} = \frac{c_{11}-c_{12}}{2} = c_{66}. \tag{10}$$

The bulk modulus is

$$K = \frac{c_{33}(c_{11}+c_{12})-2c_{13}^2}{c_{11}+c_{12}-4c_{13}+2c_{33}} \tag{11}$$

and Poisson's ratio for loading along the polar axis is

$$\nu_{LT} = \nu_{zx} = \frac{c_{13}}{c_{11}+c_{12}}. \tag{12}$$

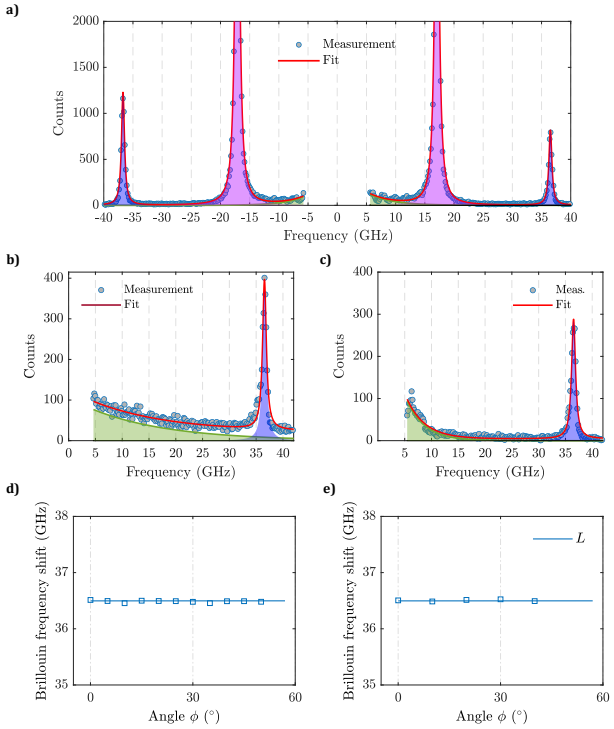

Figure 4. E-glass fiber. Experimental BLS spectra are recorded (a) along the Z axis (at incidence angle $\phi = 90°$), and at incidence angle $\phi = 20°$ in (b) the (XZ) and (c) the (XY) planes. They are well represented by a fitting function (red line) defined as the sum of Lorentzian shapes (blue and purple colors) and an exponential function (green color). The Brillouin peaks at ± 16.8 GHz in panel (a) are for the L phonon of epoxy. The Brillouin peaks at ± 36.4 GHz in panels (a-c) are for the L phonon of E-glass. Brillouin frequency shifts are plotted versus incidence angle ϕ in (d) the (XZ) and (e) the (XY) plane. Experimental points are shown with square markers in all panels.

3. Results and Discussion

3.1. E-glass fiber

As previously noted, E-glass fiber is isotropic and only the elastic constant c_{11} is accessible with micro-BLS in the backscattering geometry. Epoxy resin is isotropic as well. The axial BLS measurement (incidence angle $\phi = 90°$) in Figure 4a shows both the Stokes (negative frequency shifts) and the anti-Stokes (positive frequency shifts) parts of the Brillouin spectrum. The spectrum evidences both the longitudinal phonons of the fiber (at ± 36.4 GHz) and of the epoxy matrix (at ± 17.1 GHz). This observation indicates that light injected in the sample at the top of the fiber is not guided by the fiber but is refracted inside the epoxy matrix. Figure 4a indicates that the experimental spectrum is well fitted with a function defined as the sum of Lorentzian shapes (one per each phonon) and an exponential function accounting for elastic (Rayleigh) scattering.

Figure 4b,c demonstrates fits to the anti-Stokes

part of the experimental Brillouin spectrum for incidence angle $\phi = 20°$ in the (XZ) and the (XY) planes, for the free standing fiber. A single longitudinal phonon is observed at the same frequency, confirming that $n_e = n_o$ in E-glass. Actually, the same measurement was repeated for a total of 16 different incidence angles, as reported in Fig. 4d,e, and the Brillouin frequency shift appears to be independent of the angle of incidence, as expected. Combining the 16 measurements, the Brillouin frequency is 36.453±0.025 GHz. The latter standard deviation gives an estimate of experimental dispersion error, assuming the same longitudinal acoustic phonon is involved for all angles of incidence. Assuming the index of refraction and the mass density to be given by the values in Table 1, the longitudinal velocity $v = 6251 \pm 4$ m s^{-1} and the elastic constant $c_{11} = 100.4 \pm 0.14$ GPa. For comparison, we note that for plate samples of soda-lime glass and fused silica, the measured longitudinal Brillouin frequencies are about 32 GHz and 33 GHz, respectively [34]. The Brillouin frequency for the E-glass fiber reported here is only slightly larger.

Note that BLS measurements are local: in our setup we collect backscattered light coming from a small volume inside the fiber of about 16 µm^3, given that the lateral resolution is about 2 µm and the axial depth of focus is about 4 µm. Furthermore, the fiber is mechanically unconstrained and the typical displacements for thermal phonons are of the order of the femtometer. Even though frequencies are rather high, strains are still very small since the phonon wavelength is $\lambda/(2n) = 170$ nm. These facts are to be kept in mind when comparing the elastic constants measured with BLS with those obtained via static or quasi-static mechanical tests, especially when large stress or strain is applied.

Perrin et al. [35] mention that the accepted value for Young's modulus for E-glass is 73 ± 2 GPa. These authors performed vibrational analysis of fibers using an electrodynamic shaker and obtained that the value of the longitudinal modulus can differ up to 26% compared to the mean value $E = 74.1$ GPa, for the second vibration mode.

Based on our fitted value for c_{11} and assuming Poisson's ratio to be 0.2 (lower bound in Table 1), relation (7) gives $E = 89.5$ GPa, which is larger than the range quoted above. Conversely, assuming $E = 74.1$ GPa would lead to $\nu = 0.3$ or the upper bound in Table 1. Hence, BLS measurement of the elastic tensor, when combined with Young's modulus measured by vibrational analysis, may lead to revised estimates of Poisson's ratio and in any case gives access to this parameter without requiring a tensile strain-stress experiment under large deformations.

3.2. PA11 fiber

The axial BLS measurement (incidence angle $\phi = 90°$) in Figure 5a shows both the Stokes and the anti-Stokes parts of the Brillouin spectrum for the PA11 fiber. The spectrum evidences both a longitudinal phonon (23.9 GHz) and a shear phonon (6.0 GHz) of the fiber and the longitudinal phonon of the epoxy matrix (17.1 GHz as in the previous section). The experimental spectrum is well fitted with a function defined as the sum of Lorentzian shapes (one per each phonon) and an exponential function accounting for elastic scattering, though the low frequency of the shear phonon makes it more difficult to resolve faithfully with the tandem Fabry-Perot interferometer.

Figure 5b,c demonstrates fits to the anti-Stokes part of the experimental Brillouin spectrum for incidence angle $\phi = 55°$ in the (XZ) and the (XY) planes, for the free standing PA11 fiber. The

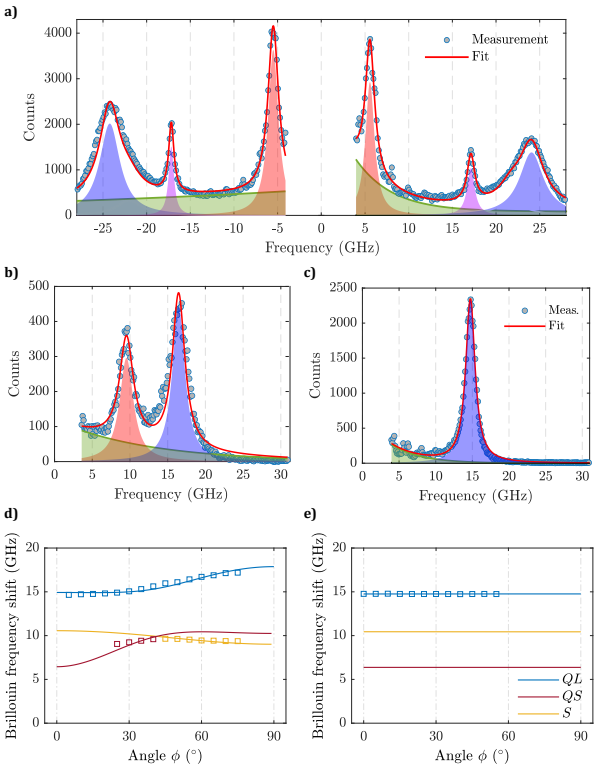

Figure 5. PA11 fiber. Experimental BLS spectra are recorded (a) along the Z axis (at incidence angle $\phi = 90°$), and at incidence angle $\phi = 55°$ in (b) the (XZ) and (c) the (XY) planes. They are well represented by a fitting function (red line) defined as the sum of Lorentzian shapes (blue, red and purple colors) and an exponential function (green color). The blue and red Lorentzians are for longitudinal and shear phonons of the PA11 fiber, respectively, and the purple Lorentzian is for the longitudinal phonon of epoxy. Brillouin frequency shifts for the PA11 fiber are plotted versus incidence angle ϕ in (d) the (XZ) and (e) the (XY) plane, and are associated with the QL, QS and S phonons of the fiber. Experimental points are shown with square markers in all panels.

Elastic constants (GPa)	c_{11}	7.13 ± 0.07
	c_{12}	0.00 ± 0.13
	c_{13}	4.03 ± 0.11
	c_{33}	18.98 ± 0.26
	c_{44}	1.33 ± 0.04
Relative permittivity	n_e^2	2.26 ± 0.03
Fit error (GHz)	e	0.17
Mechanical properties	E_L	14.42 ± 0.39 GPa
	E_T	6.16 ± 0.15 GPa
	c_{66}	3.56 ± 0.08 GPa
	K	3.55 ± 0.08 GPa
	ν_{LT}	0.56 ± 0.02

Table 2. Fitted material constants and derived mechanical properties for the PA11 fiber.

measurements confirm the anisotropic character of the PA11 fiber, since the Brillouin frequency shift depends on the angle of incidence. One longitudinal wave with a frequency of 16.43 GHz and one shear wave with a frequency of 9.54 GHz are observed in the (XZ) plane. In the case of wave propagation perpendicular to the fiber axis, in plane (XY), only the longitudinal phonon at 14.74 GHz is detected.

Table 2 reports the mechanical and optical properties obtained by fitting against the transversely isotropic model. Assuming $n_o = 1.52$, the birefringence is estimated as $\Delta n = n_e - n_o = -0.017 \pm 0.003$. This value induces a change of about 1% in the Brillouin frequency of the QL phonon for $\phi = 0°$ that is detectable with respect to the spectral resolution ($\sim$ 120 MHz). In the case of Nylon 11, optical anisotropy arises from the molecular alignment of the fiber. This is often observed in anisotropic materials such as certain polymers when they are stretched or aligned during processing. Nylon 11, being a semi-crystalline polymer, can develop birefringence due to the alignment of its polymer chains during processes like drawing or extrusion. This phenomenon is well documented in various types of nylon fibers, including Nylon 6 [36, 37] and Nylon 6.6 [38, 37], and similar behavior can be expected in Nylon 11 fibers due to their similar molecular structure and processing methods. According to Balcerzyk et al. [37] the birefringence of Nylon fibers spans the range $\Delta n = [0 - 0.0194]$, in agreement with the value obtained here.

We emphasize the more than two-fold difference between axial (c_{33}) and radial (c_{11}) elastic constants for longitudinal motion. A comparison between phonon velocity curves obtained using the fitted elastic constants and experiment is proposed in Figure 6. As a note, we decided to attribute experimental peaks to different shear phonons (QS if $\phi < 45°$ and S above). This choice of the slowest phonon is made because the

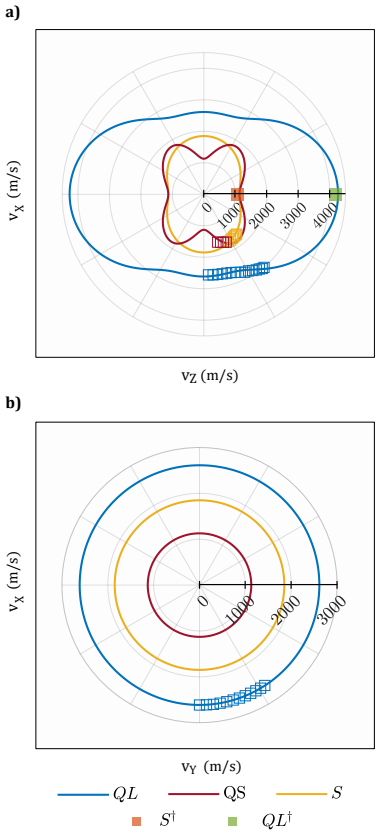

Figure 6. Velocity curves for the PA11 fiber in (a) the (XZ) and (b) the (XY) plane. Experimental velocities obtained with the free-standing fiber are shown with open square markers. The experimental S and QL velocities obtained with the fiber-in-epoxy sample are shown with filled square markers in (a). Solid lines are for theoretical velocity curves obtained from the fitted material constants.

two velocity curves cross between $\phi = 40°$ and $\phi = 45°$. It was checked numerically that the fit error is smaller with this choice compared to any other permutation of the classification.

Turning to the transformed mechanical properties, the longitudinal modulus of PA11 in this study is measured to be 14.4 GPa, significantly larger than previously reported values that are in the range of $1 - 1.3$ GPa [39, 8], but are obtained from quasi-static mechanical tests. The discrepancy is, however, consistent with values commonly obtained from BLS measurements in polymers [40]. Furthermore, the Young's modulus for the IP-S photoresin, estimated through the analysis of beam resonances in the MHz frequency range, has been reported to be 10 GPa for frequencies between 1 and 3 MHz [41]. The viscoelastic properties of organic materials are indeed inherently frequency-dependent, as such materials exhibit a combination of elastic (solid-like) and viscous (fluid-like) behaviors that shift based on the frequency of applied stress or strain. As a combination of viscous

and elastic effects, the apparent elastic modulus increases with frequency. This variation in elastic modulus with frequency reflects the interplay between elasticity and viscosity, making it critical for accurately characterizing viscoelastic materials under dynamic loading conditions.

At longitudinal strain of 0.5%, the apparent Poisson's ratio of Nylon monofilament yarn was found to be in the range $\nu_{LT} = [0.35 - 0.45]$ [9]. In the case of nanocomposite modeling, a value often used for Poisson's ratio is 0.35 according to [10]. Zhang et al. [11] reported that the Poisson's ratios of various synthetic polymer fibers, including Kevlar, Nylon 6, and PBO (poly (p-phenylene-2, 6-benzobisoxazole), fall within the range of $\nu_{LT} = [0.34 - 0.50]$. The BLS technique here estimates this value to be 0.56.

3.3. Silk fiber

The axial BLS measurement (incidence angle $\phi = 90°$) in Figure 7a shows both the Stokes and the anti-Stokes parts of the Brillouin spectrum for the silk fiber. The spectrum evidences both a longitudinal phonon (25.4 GHz) and a shear phonon (10.6 GHz) of the fiber and the longitudinal phonon of the epoxy matrix. The experimental spectrum is well fitted with a function defined as the sum of Lorentzian shapes (one per each phonon) and an exponential function accounting for elastic scattering.

Figure 7b,c presents an example of a fit to the measurements for an incident angle $\phi = 25°$ in the (XZ) and the (XY) planes. A longitudinal phonon is propagating with a frequency of 18.90 GHz and a shear phonon at 11.10 GHz in the anisotropic (XZ) plane, whereas in the isotropic (XY) plane only a longitudinal phonon with frequency 18.27 GHz is propagating.

Table 3 reports the mechanical and optical properties obtained by fitting against the transversely isotropic model. Our result for synthetic silk indicates $n_e = 1.5232 \pm 0.0066$ and thus a negative birefringence $\Delta n = -0.0355$ with the same accuracy. As for the PA11 fiber, the sign of the birefringence is obtained from the frequencies of the QL phonons in different incidence planes. According to Little et al. [14], refractive index measurements of radial silks spanned from 1.5370 ± 0.0013 to 1.5596 ± 0.0008, illustrating a variability of approximately 1.5% in the refractive index of natural silk fibers. Significant birefringence, both positive and negative, reaching up to $\Delta n = 0.0129 \pm 0.0007$, was observed in certain silks, while others showed no discernible birefringence. Wang et al. [4] reported the birefringence of spider silk obtained from experiments performed in transmission BLS geometry as $\Delta n = 0.06$, with $n_e = 1.46 \pm 0.02$ and $n_o = 1.40 \pm 0.01$.

The elastic constants for natural silk are larger by a factor two compared to those of PA11, approximately. c_{33} is almost twice as large as c_{11}. The velocity curves for shear phonons again cross. Direction-dependent sound velocities for the natural silk fiber are represented in Fig. 8.

Using in situ tensile tests and x-ray diffraction, Krasno et al. [42] determined the mechanical properties of the crystalline and disordered phases of silk by adapting a linear viscoelastic model to its semi-crystalline morphology. They observed a strong interplay between morphology and mechanical properties, with silk's high extensibility primarily resulting from the disordered phase. A linear fit of the stress-strain curve for the fibroin crystals in silkworm silk consistently yielded a purely elastic modulus of $E = 26.5 \pm 0.8$ GPa from the slope. This value is in fair agreement with our experiment using micro-BLS technique giving $E_L = 19$ GPa. Spider and silkworm

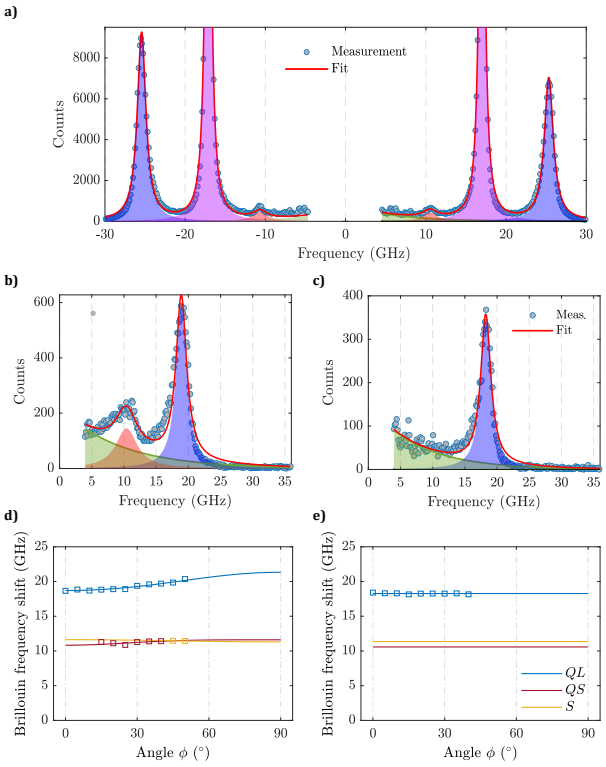

Figure 7. Silk fiber. Experimental BLS spectra are recorded (a) along the Z axis (at incidence angle $\phi = 90°$), and at incidence angle $\phi = 25°$ in (b) the (XZ) and (c) the (XY) planes. They are well represented by a fitting function (red line) defined as the sum of Lorentzian shapes (blue, red and purple colors) and an exponential function (green color). The blue and red Lorentzians are for longitudinal and shear phonons of the silk fiber, respectively, and the purple Lorentzian is for the longitudinal phonon of epoxy. Brillouin frequency shifts for the silk fiber are plotted versus incidence angle ϕ in (d) the (XZ) and (e) the (XY) plane, and are associated with the QL, QS and S phonons of the fiber. Experimental points are shown with square markers in all panels.

Elastic constants (GPa)	c_{11}	14.26 ± 0.07	
	c_{12}	3.24 ± 0.22	
	c_{13}	8.05 ± 0.12	
	c_{33}	26.39 ± 0.25	
	c_{44}	4.78 ± 0.04	
Relative permittivity	n_e^2	2.32 ± 0.01	
Fit error (GHz)	e	0.03	
Mechanical properties	E_L	18.98 ± 0.34	GPa
	E_T	11.75 ± 0.17	GPa
	c_{66}	5.51 ± 0.11	GPa
	K	8.72 ± 0.11	GPa
	ν_{LT}	0.46 ± 0.01	

Table 3. Fitted material constants and derived mechanical properties for the silk fiber.

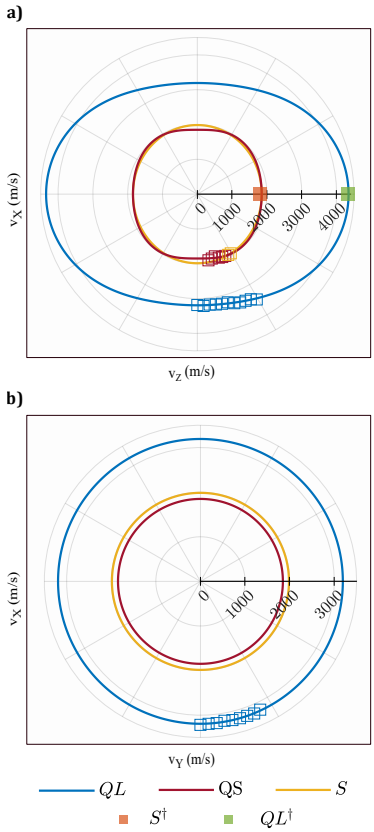

Figure 8. Velocity curves for the silk fiber in (a) the (XZ) and (b) the (XY) plane. Experimental velocities obtained with the free-standing fiber are shown with open square markers. The experimental S and QL velocities obtained with the fiber-in-epoxy sample are shown with filled square markers in (a). Solid lines are for theoretical velocity curves obtained from the fitted material constants.

silk fibers exhibit morphological similarities as semi-crystalline nanocomposites, featuring ordered regions composed of β-sheet protein nanocrystals embedded within a softer matrix of disordered material (spider silk [43], silkworm fibroin [44]).

Although BLS measurements on synthetic silk fibers have not been documented, the longitudinal modulus of 19 GPa and the transverse Young's modulus of 11.7 GPa obtained in this work match the values obtained via BLS reported by Wang et al. [4] for spider silk, which are 20.9 GPa and 9.2 GPa, respectively. In the natural state of silkworm silk fiber, furthermore, the longitudinal and the transverse Young's moduli of 23.4±1.0 and 10.4±0.5 GPa, as well as shear modulus $G = 4.5 \pm 0.2$ GPa, were measured by BLS by Aluculesei et al. [5]. Our values for synthetic silk fiber thus align well with those for natural silk fiber.

The remarkable strength of silkworm and spider silks is attributed to β-sheet nanocrystals that rely on hydrogen bonds, considered among the weakest chemical bonds. Keten et al. [45] employed large-scale molecular dynamics simulations and demonstrated that β-sheet nanocrystals confined to nanometer scales exhibit superior stiffness, strength, and mechanical toughness compared to larger nanocrystals. In addition to analyzing shear contributions relative to nanocrystal size, Keten et al. [45] estimated the material's elastic moduli to be $E = 22.6$ GPa and $G = 4.6$ GPa from bending and shear rigidity, respectively. Density functional theory (DFT) calculations confirmed their findings, yielding slightly higher values ($E = 36.45$ GPa and $G = 10.32$ GPa), as expected for static calculations at zero temperature. Their results align well with reported experimental elastic moduli values for spider-silk nanocrystals $E = [16-28]$ GPa [42, 46]. While direct testing of the shear modulus of silk β-sheet nanocrystals is lacking, torsion experiments on silk fibers suggest similar shear moduli ($G = 2.38$ GPa for Nephila clavipes dragline silk and $G = 3.81$ GPa for Bombyx morisilk).

The Poisson's ratio of the silk fiber is found to be 0.46 in this work, whereas Fraternali et al. [13] report the range $\nu = [0.1-0.4]$ for a spider dragline silk. As a note, Aluculesei et al. [5] determined the Poisson ratio for Bombyx mori silkworm silk fiber to be $\nu = 0.51$ by BLS.

3.4. Flax fiber

The axial BLS measurement (incidence angle $\phi = 90°$) in Figure 9a shows both the Stokes and the anti-Stokes parts of the Brillouin spectrum for the flax fiber. The spectrum evidences both a longitudinal phonon (53.0 GHz) and a shear phonon (10.6 GHz) of the fiber and the longitudinal phonon of the epoxy matrix. The experimental spectrum is well fitted with a function defined as the sum of Lorentzian shapes (one per each phonon) and an exponential function accounting for elastic scattering.

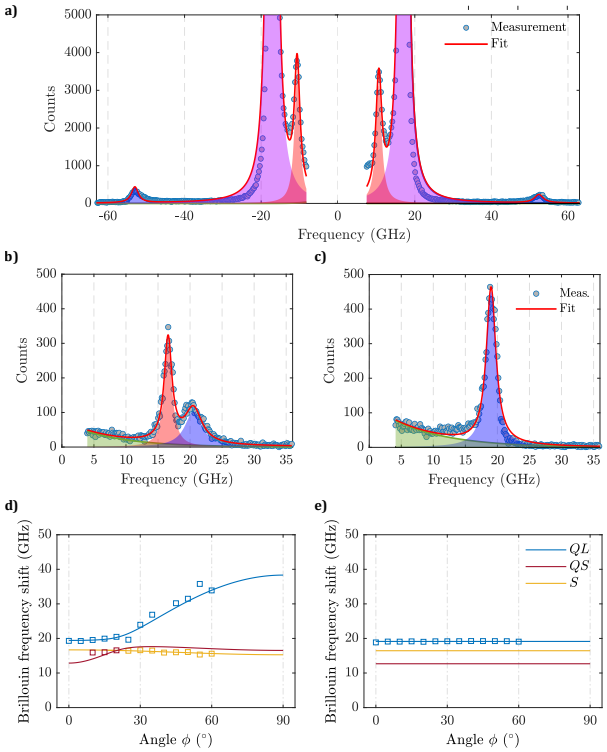

Figure 9. Flax fiber. Experimental BLS spectra are recorded (a) along the Z axis (at incidence angle $\phi = 90°$), and at incidence angle $\phi = 20°$ in (b) the (XZ) and (c) the (XY) planes. They are well represented by a fitting function (red line) defined as the sum of Lorentzian shapes (blue, red and purple colors) and an exponential function (green color). The blue and red Lorentzians are for longitudinal and shear phonons of the flax fiber, respectively, and the purple Lorentzian is for the longitudinal phonon of epoxy. Brillouin frequency shifts for the flax fiber are plotted versus incidence angle ϕ in (d) the (XZ) and (e) the (XY) plane, and are associated with the QL, QS and S phonons of the fiber. Experimental points are shown with square markers in all panels.

Figure 9b,c presents an example of a fit to the measurements for an incidence angle $\phi = 20°$ in the (XZ) and the (XY) planes. In the (XZ) plane one longitudinal wave with a frequency of 20.46 GHz and one shear wave with a frequency of 16.56 GHz are observed. In the case of wave propagation perpendicular to the fiber axis, in plane (XY), only the longitudinal phonon at 19.03 GHz is detected. The characteristics of the observed phonons are similar to the case of the PA11 and the silk fibers.

Table 4 reports the mechanical and optical properties obtained by fitting against the transversely isotropic model. The birefringence of the flax fiber is estimated as $\Delta n = n_e - n_o = -0.024 \pm 0.019$. Paterson et al. [47] used polarized light microscopy (PLM) to examine the refractive indices of flax fibers. The birefringence values obtained in their study are similar to ours, though they quote a positive sign for the birefringence and $\Delta n = 0.065$. Strikingly, the value

Elastic constants (GPa)	c_{11}	16.0	$\pm$ 0.6
	c_{12}	-7.6	$\pm$ 1.0
	c_{13}	6.0	$\pm$ 2.8
	c_{33}	143.3	$\pm$ 4.6
	c_{44}	7.0	$\pm$ 0.4
Relative permittivity	n_e^2	2.42	$\pm$ 0.11
Fit error (GHz)	e	2.0	
Mechanical properties	E_L	134.8	$\pm$ 9.4 GPa
	E_T	11.9	$\pm$ 3.9 GPa
	c_{66}	11.9	$\pm$ 0.6 GPa
	K	4.18	$\pm$ 0.6 GPa
	ν_{LT}	0.7	$\pm$ 0.35

Table 4. Fitted material constants and derived mechanical properties for the flax fiber.

of c_{33} is found to be almost ten times as large as c_{11}. This large variation is accompanied by a negative value for c_{12}, resulting in $c_{66} = (c_{11} - c_{12})/2 = 11.9$ GPa. The determination of elastic constants enables plotting the velocity curves in Figure 10. Those demonstrate a very anisotropic dependence of phonon velocities. The velocity curves in Figure 10a are reminiscent of the strong anisotropy of structural composites, as embodied by phononic crystals considered as acoustic metamaterials [28].

Reported values for Young's modulus of flax fibers range from 20 GPa to 160 GPa [27, 48, 17, 18, 26, 49, 50]. Due to the frequency-dependence of the apparent viscoelastic properties of organic materials, as mentioned above, our BLS value is clearly in the upper range. Flax fibers have a transverse section that is not only nonuniform but also contains the lumen. With the backscattering Brillouin technique, a volume of about 16 cubic micrometers is probed, and the response integrates all the fiber wall layers, resulting in a homogenized response at the phonon wavelength scale. A decrease in Young's modulus with increasing fiber diameter has been observed in flax fibers [27]. This reduction in mechanical properties was partially attributed to the presence of the lumen at the fiber's center, which enlarges as the fiber diameter increases. The lumen size is often excluded from cross-sectional calculations due to the difficulty in accurately determining its dimensions. As a note, it is however included in the value of the mass density given in Table 1 [15]. Richely et al. [26] investigated the diameter dependence of Young's modulus in elementary hemp fibers using a mathematical model. They found that the surface area proportion of the lumen does not exhibit a positive dependency on fiber diameter, suggesting that Bourmaud et al.'s [27] assumption could only partially explain the modulus-diameter relationship.

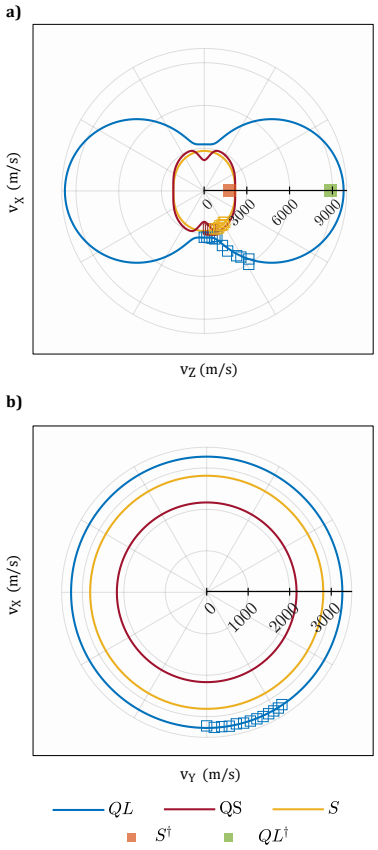

Figure 10. Velocity curves for the flax fiber in (a) the (XZ) and (b) the (XY) plane. Experimental velocities obtained with the free-standing fiber are shown with open square markers. The experimental S and QL velocities obtained with the fiber-in-epoxy sample are shown with filled square markers in (a). Solid lines are for theoretical velocity curves obtained from the fitted material constants.

As a note, a recent report estimates $c_{33} = 47$ GPa for a flax fiber, from a single BLS measurement in the 90a-scattering geometry [51] – different from our 180a or backscattering geometry. This is almost three times less than the value we find. The origin of the discrepancy remains unclear to us, but since we have not used the same samples and scattering geometries, a precise comparison can only be left as a perspective. Finally, we observe that the Poisson's ratio obtained in our study, using the micro-BLS technique, is 0.7 with a rather large standard deviation. The range of values reported in the literature spans from 0.2 to 0.5 [16, 17, 18]. The large standard deviation of our estimate notably originates from the uncertainty associated with the estimation of c_{13}. Unfortunately, this uncertainty is connected to the range of available incidence angles and could not be reduced for the flax fiber.

3.5. Final remarks

The components of the elastic tensor of a material must satisfy certain stability constraints to ensure that any deformation increases the strain energy potential. For transversely isotropic materials these conditions read [3] $c_{11} > |c_{12}|$, $(c_{11}+c_{12})c_{33} > 2c_{13}^2$, and $c_{44} > 0$. These stability inequalities are satisfied for the flax fiber as well as for the other fibrous materials measured in this work.

The accuracy of the fit procedure used for the anisotropic fibers depends on the available set of experimentally observable Brillouin peaks. In order to obtain BLS measurements of shear and longitudinal phonons propagating along the axis of the fibers, we had to rely on samples with the fiber embedded in an epoxy matrix. Those measurements significantly and directly improve the estimation of elastic constants c_{33} and c_{44}. Other incidence angles were obtained with free-standing fibers. For incidence normal to the fiber axis, only the elastic constant c_{11} is involved but additional information on the birefringence is gained as well. Information on elastic constants c_{13} and c_{12} (or equivalently c_{66}) is provided by varying the angle of incidence in the (XZ) plane. As a perspective, it would be interesting to prepare free-standing samples that can be measured both axially and from the side, since this would allow one to obtain the elastic tensor for a single sample.

4. Conclusions

The elastic properties of E-glass, silk, PA11 and flax fiber samples were investigated using micro-Brillouin light scattering. The methodology involves performing multi-angle backscattering measurements in different incidence planes, accounting for optical birefringence, and carefully assigning phonon modes. All material constants were fitted against the transversely-isotropic model, except for E-glass fiber that was checked to be isotropic. Comparison of simulation and experimental data reveals a clear agreement with the symmetry-driven models. Limitations in the methodology arise from the need to assume the value of one of the indices of refraction and of the material density. The accuracy with which these constants are known directly translates into a possible bias for elastic constants. That limitation aside, elastic constants can be assessed precisely, without contact, and locally. The micro-Brillouin light scattering approach thus holds promise for extension to other synthetic and natural materials with known orientation and symmetry.

Acknowledgments

The authors acknowledge Linificio e Canapificio Nazionale for providing silk fibers and the University of South Britany for providing PA11 fibers. FP and PB acknowledge the support of the French Agence Nationale de la Recherche (ANR), under grant ANR-22-CE51-0001 (proje-ct MIDIFIC). This work has been supported by the EIPHI Graduate school (grant ANR-17-EURE-0002) and by the Bourgogne-Franche-Comté Region. Support from the French RENATECH network and its FEMTO-ST technological facility is gratefully acknowledged.

Author contributions: CRediT

Fehima Ugarak: Conceptualization, Software, Formal analysis, Investigation, Data Curation, Writing - Original Draft, Visualization. **Fanny Pelisson**: Resources, Writing - Review & Editing. **Marina Raschetti**: Investigation, Writing - Review & Editing. **Vincent Placet**: Resources, Writing - Review & Editing, Supervision. **Pauline Butaud**: Resources, Writing - Review & Editing, Supervision, Funding acquisition. **Morvan Ouisse**: Resources, Writing - Review & Editing, Supervision. **Alexis Mosset**: Validation, Writing - Review & Editing, Supervision. **Vincent Laude**: Conceptualization, Methodology, Software, Writing - Original Draft, Supervision, Funding acquisition.

Appendix A. Group of symmetry

The group of symmetry for wave propagation along a fiber is $A\infty$, which means revolution symmetry or transverse isotropy. According to the tables of crystallography [52], if axis x_3 is the axis of revolution, the symmetric elastic tensor assumes the following shape

$$c_{\alpha\beta} = \begin{pmatrix} c_{11} & c_{12} & c_{13} & 0 & 0 & 0 \\ c_{12} & c_{11} & c_{13} & 0 & 0 & 0 \\ c_{13} & c_{13} & c_{33} & 0 & 0 & 0 \\ 0 & 0 & 0 & c_{44} & 0 & 0 \\ 0 & 0 & 0 & 0 & c_{44} & 0 \\ 0 & 0 & 0 & 0 & 0 & c_{66} \end{pmatrix} \tag{A.1}$$

with $c_{12} = c_{11} - 2c_{66}$. There are 5 independent constants The shape of the elastic tensor is thus the same as for hexagonal crystals with point group 6, $\bar{6}$ or $6/m$.

The shape of the photoelastic tensor is more complicated, since it is not symmetrical:

$$p_{\alpha\beta} = \begin{pmatrix} p_{11} & p_{12} & p_{13} & 0 & 0 & p_{16} \\ p_{12} & p_{11} & p_{13} & 0 & 0 & -p_{16} \\ p_{31} & p_{31} & p_{33} & 0 & 0 & 0 \\ 0 & 0 & 0 & p_{44} & p_{45} & 0 \\ 0 & 0 & 0 & -p_{45} & p_{44} & 0 \\ -p_{16} & p_{16} & 0 & 0 & 0 & p_{66} \end{pmatrix} \tag{A.2}$$

with $p_{12} = p_{11} - 2p_{66}$. There are 8 independent photoelastic constants.

Appendix B. Christoffel equation

The reference frame (x_1, x_2, x_3) is here taken as the crystallographic frame (X, Y, Z). We consider incidence in the (13) plane, with angle of incidence ϕ defined with respect to axis 1. The direction of incidence (propagation) is thus $[c, 0, s] = [\cos\phi, 0, \sin\phi]$. The Christoffel tensor is

$$\Gamma_{il} = \begin{pmatrix} c^2c_{11} + s^2c_{44} & 0 & sc(c_{13} + c_{44}) \\ 0 & c^2c_{66} + s^2c_{44} & 0 \\ sc(c_{13} + c_{44}) & 0 & c^2c_{44} + s^2c_{33} \end{pmatrix} \tag{B.1}$$

There are thus three eigenvalues and eigenvectors yielding the possible bulk acoustic phonons. There is one pure shear wave, denoted by S and polarized along axis 2 for all angles of incidence. That wave produces S_4 and S_6 strains. The pure shear velocity $\sqrt{(c^2c_{66} + s^2c_{44})/\rho}$ depends on c_{44} and c_{66}. There is also one (QL, QS) pair of waves, polarized in the $(1, 3)$ plane. Those waves produce S_1, S_3 and S_5 strains. Putting $\Delta = (\Gamma_{11} - \Gamma_{33})^2 + 4\Gamma_{13}^2$, the QL velocity is $\sqrt{\frac{1}{2}(\Gamma_{11} + \Gamma_{33} + \sqrt{\Delta})/\rho}$ and the QS velocity is $\sqrt{\frac{1}{2}(\Gamma_{11} + \Gamma_{33} - \sqrt{\Delta})/\rho}$. Both velocities depend on c_{11}, c_{44}, c_{13} and c_{33}.

Appendix C. Photoelastic coupling

We don't know the numerical values of the photoelastic constants, but can we anyway understand which phonons are seen in the experiments from symmetry considerations? The H direction is imposed to be axis 2 by the interferometer. The V direction is then in the plane $(1, 3)$, orthogonal to the direction of incidence, hence given by $[-s, 0, c]$. As a result, we have the possibilities

- HH: $\alpha = 2$ only,
- HV: $\alpha = 4$ or 6.

If incidence is along [100], then in this case $c = 1$ and $s = 0$. H direction is axis 2, V direction is axis 3. Hence HV corresponds to $\alpha = 4$ only. The possible photoelastic couplings are summarized in Table C1.

	HH ($\alpha = 2$)	HV ($\alpha = 4$)
QL ($\beta = 1$)	$p_{21} \neq 0$	$p_{41} = 0$
QS ($\beta = 5$)	$p_{25} = 0$	$p_{45} \ll 1$
S ($\beta = 6$)	$p_{26} \ll 1$	$p_{46} = 0$

Table C1. Possible photoelastic couplings for incidence along direction [100].

Since no shear phonons are observed in experiments for direction [100], we conclude that $p_{45} \ll 1$ and $p_{26} \ll 1$. The photoelastic tensor then simplifies to a form similar to hexagonal crystals:

$$p_{\alpha\beta} = \begin{pmatrix} p_{11} & p_{12} & p_{13} & 0 & 0 & \approx 0 \\ p_{21} & p_{11} & p_{13} & 0 & 0 & \approx 0 \\ p_{31} & p_{31} & p_{33} & 0 & 0 & 0 \\ 0 & 0 & 0 & p_{44} & \approx 0 & 0 \\ 0 & 0 & 0 & \approx 0 & p_{44} & 0 \\ \approx 0 & \approx 0 & 0 & 0 & 0 & p_{66} \end{pmatrix} \quad \text{(C.1)}$$

	HH ($\alpha = 2$)	HV ($\alpha = 6$)
QL ($\beta = 3$)	$p_{23} \neq 0$	$p_{63} = 0$
QS ($\beta = 5$)	$p_{25} = 0$	$p_{65} = 0$
S ($\beta = 4$)	$p_{24} = 0$	$p_{64} = 0$

Table C2. Possible photoelastic couplings for incidence along direction [001].

If incidence is along [001], then in this case $c = 0$ and $s = 1$. H direction is axis 2, V direction is axis 1. Hence HV corresponds to $\alpha = 6$ only. The possible photoelastic couplings are summarized in Table C2. This time, we unexpectedly see experimentally a shear phonon when the photoelastic coupling is exactly zero for plane wave incidence. To solve the apparent paradox, we assume that for incidence slightly different from $s = 1$, we have some HV polarization along axis 3 as well, or $\alpha = 4$, because of the finite numerical aperture. In this case the S shear phonon is associated with $p_{44} \neq 0$. The same reasoning for incidence along axis 1 leads to the conclusion that $p_{66} \ll 1$, because no shear phonon is observed in this case.

Finally, in the general case of incidence along $[c, 0, s]$, the possible photoelastic couplings are summarized in Table C3.

	HH ($\alpha = 2$)	HV ($\alpha = 4, 6$)
QL/QS ($\beta = 1, 3, 5$)	p_{21}, p_{23}	0
S ($\beta = 4, 6$)	0	p_{44}

Table C3. Possible photoelastic couplings for incidence along direction $[c, 0, s]$.

Combining these results with the analytical shapes of the velocity curves lead to the following observations regarding the fit process. Elastic constants c_{33} and c_{44} are strongly determined by axial measurements ($s = 1$). Elastic constant c_{11} is strongly determined by measurements orthogonal to the fiber axis ($c = 1$). The remaining independent elastic constants c_{12} (or c_{66}) and c_{13} are determined by measurements with intermediate incidence angles; c_{66} is determined by S phonon velocities and c_{13} is determined by QL/QS phonon velocities.

References

[1] Elsayad K, Urstöger G, Czibula C, Teichert C, Gumulec J, Balvan J, Pohlt M and Hirn U 2020 *Cellulose* **27** 4209–4220

[2] Fioretto D, Caponi S and Palombo F 2019 *Biomedical Optics Express* **10** 1469–1474

[3] Czibula C, Ulz M H, Wagner A, Elsayad K, Hirn U and Koski K J 2024 *Journal of Physics: Photonics* **6** 035012

[4] Wang Z, Cang Y, Kremer F, Thomas E L and Fytas G 2020 *Biomacromolecules* **21** 1179–1185

[5] Aluculesei A, Zhang Y, Huang S, Wang Z, Cang Y, Min Y and Fytas G 2025 *Biomacromolecules* **26** 2479–2486

[6] E-glass fiber, generic accessed: 2024-08-26 URL `https://www.matweb.com/search/DataSheet.aspx?MatGUID=d9c18047c49147a2a7c0b0bb1743e812&ckck=1`

[7] Agarwal B D, Broutman L J and Chandrashekhara K 2017 *Analysis and performance of fiber composites* (John Wiley & Sons)

[8] Polyamide 11 accessed: 2024-06-27 URL `https://designerdata.nl/materials/plastics/thermo-plastics/polyamide-11`

[9] Takatera M, Arichi T, Peiffer J, Zhu C and Kim K 2017 *Textile Research Journal* **87** 739–746

[10] Halim K A A, Kennedy J E, Salleh M A A M, Osman A F, Omar M F and Sunar N M 2023 *Archives of Metallurgy and Materials* **68** 1349–1355

[11] Zhang K, Si F W, Duan H L and Wang J 2010 *Acta biomaterialia* **6** 2165–2171

[12] Babu K M 2018 *Silk: processing, properties and applications* (Woodhead Publishing)

[13] Fraternali F, Stehling N, Amendola A, Tiban Anrango B A, Holland C and Rodenburg C 2020 *Nanomaterials* **10** 1510

[14] Little D J and Kane D M 2011 *Optics Express* **19** 19182–19189

[15] Amiri A, Triplett Z, Moreira A, Brezinka N, Alcock M and Ulven C A 2017 *Industrial Crops and Products* **96** 196–202

[16] Sliseris J, Yan L and Kasal B 2016 *Composites part B: Engineering* **89** 143–154

[17] Modniks J and Andersons J 2010 *Computational Materials Science* **50** 595–599

[18] Scida D, Bourmaud A and Baley C 2017 *Materials & Design* **122** 136–145

[19] Flax fiber cross-section accessed: 2024-08-26 URL `http://wwww.microlabgallery.com/gallery/Flax3bXSecfixed.aspx`

[20] Lao S C, Yong W, Nguyen K, Moon T J, Koo J H, Pilato L and Wissler G 2010 *Journal of Composite Materials* **44** 2933–2951

[21] Becker N, Oroudjev E, Mutz S, Cleveland J P, Hansma P K, Hayashi C Y, Makarov D E and Hansma H G 2003 *Nature Materials* **2** 278–283

[22] Shao Z and Vollrath F 2002 *Nature* **418** 741–741

[23] Vollrath F and Knight D P 2001 *Nature* **410** 541–548

[24] Flax fibre: Types, chemical composition, properties and uses accessed: 2024-07-

02 URL `https://textileengineering.net/flax-fibre-types-properties-and-uses/`
[25] Li H, Tang R, Dai J, Wang Z, Meng S, Zhang X and Cheng F 2022 *Advanced Fiber Materials* **4** 171–184
[26] Richely E, Bourmaud A, Placet V, Guessasma S and Beaugrand J 2022 *Progress in Materials Science* **124** 100851
[27] Bourmaud A, Morvan C and Baley C 2010 *Industrial Crops and Products* **32** 662–667
[28] Laude V, Iglesias Martínez J A, Wang Y F and Kadic M 2021 *Journal of Applied Physics* **129** 215106
[29] Cusack S and Miller A 1979 *Journal of Molecular Biology* **135** 39–51
[30] Palombo F, Winlove C P, Edginton R S, Green E, Stone N, Caponi S, Madami M and Fioretto D 2014 *Journal of The Royal Society Interface* **11** 20140739
[31] Ugarak F, Iglesias Martínez J A, Mosset A and Laude V 2023 *Journal of Applied Physics* **134** 185103
[32] Nye J F 1985 *Physical properties of crystals: their representation by tensors and matrices* (Oxford university press)
[33] Ryu M, Cang Y, Wang Z, Fytas G and Morikawa J 2019 *The Journal of Physical Chemistry C* **123** 17148–17154
[34] Ugarak F, Mosset A and Laude V 2025 *Journal of Applied Physics* **137** 223103
[35] Perrin D, Alteirac M, Corn S and Shanahan M E R 2007 *Composites Part A: Applied Science and Manufacturing* **38** 71–79
[36] Nagatoshi F and Arakawa T 1970 *Polymer Journal* **1** 685–690
[37] Balcerzyk E, Kozłowski W, Wesołwska E and Lewaszkiewicz W 1981 *Journal of Applied Polymer Science* **26** 2573–2580
[38] Cannon C G, Chappel F P and Tidmarsh J I 1963 *Journal of the Textile Institute Transactions* **54** T210–T221
[39] Rouway M, Nachtane M, Tarfaoui M, Chakhchaoui N, Omari L H, Fraija F and Cherkaoui O 2020 Prediction of mechanical performance of natural fibers polypropylene composites: a comparison study *IOP Conference Series: Materials Science and Engineering* vol 948 (IOP Publishing) p 012031
[40] Ugarak F, Ulliac G, Iglesias Martínez J A, Moughames J, Laude V, Kadic M and Mosset A 2022 *Materials* **15** 4070
[41] Iglesias Martínez J A, Moughames J, Ulliac G, Kadic M and Laude V 2021 *Applied Physics Letters* **118** 063507
[42] Krasnov I, Diddens I, Hauptmann N, Helms G, Ogurreck M, Seydel T, Funari S S and Müller M 2008 *Physical Review Letters* **100** 048104
[43] Grubb D T and Jelinski L W 1997 *Macromolecules* **30** 2860–2867
[44] Shen Y, Johnson M A and Martin D C 1998 *Macromolecules* **31** 8857–8864
[45] Keten S, Xu Z, Ihle B and Buehler M J 2010 *Nature Materials* **9** 359–367
[46] Cunniff P M, Fossey S A, Auerbach M A, Song J W, Kaplan D L, Adams W W, Eby R K, Mahoney D and Vezie D L 1994 *Polymers for Advanced Technologies* **5** 401–410
[47] Paterson R A, Lowe B J, Smith C A, Lord J M and Ngarimu-Cameron R 2017 *Archaeometry* **59** 965–979
[48] Charlet K, Jernot J P, Gomina M, Bizet L and Bréard J 2010 *Journal of Composite Materials* **44** 2887–2896
[49] Thuault A, Bazin J, Eve S, Breard J and Gomina M 2014 *Journal of Industrial Textiles* **44** 22–39
[50] Baley C 2002 *Composites Part A: Applied Science and Manufacturing* **33** 939–948
[51] Pachernegg-Mair L, Schaubeder J B, Brandberg A, Thoman M, Urstöger G, Rüggeberg M, Koski K J, Plank H, Hirn U, Spirk S and Czibula C 2025 *Materials Science and Engineering: A* **942** 148675
[52] Authier (Editor) A 2014 *International Tables for Crystallography, Volume D: Physical Properties of Crystals, 2nd Edition* (Wiley)